Detached Eddy Simulation of Supersonic Wing-Elevon Cove Boundary-Layer Ingestion

Robert A. Alviani*, Jonathan Poggie †, and Gregory Blaisdell ‡
Purdue University, West Lafayette, IN, 47907

A computational investigation of wing-elevon cove fluid dynamics was done with improved delayed detached eddy simulation (IDDES). This investigation models an experimental study conducted by Deveikis and Bartlett [1], which simulated the windward surface of the space shuttle orbiter. Flow conditions correspond to high Reynolds number, fully turbulent, supersonic flow. Comparison of mean surface pressure and heat-flux between computational and experimental results show moderate discrepancies. Flow structure is visualized through mean and instantaneous streamwise contours. Flow was observed to diverge at reattachment, associated with boundary-layer ingestion into the cove. Instantaneous density gradient contours in the region display low-frequency unsteadiness of the reattaching shear-layer and shock-foot oscillation, producing distortions in the reattachment bow-shock. Large coherent turbulent structures were observed in the spanwise surface-normal plane, which appear to consist of periodic Görtler-type vortices. The unsteady behavior of the flow produces large variation in magnitude and location of peak surface heat-flux. As a result, the wing-elevon juncture and cove environment is subject to aerothermal loading on interior and exterior surfaces.

Nomenclature

$\tilde{d}$	=	DES length-scale
f_s	=	Sampling frequency
M	=	Mach number
P	=	Pressure
q	=	Dynamic pressure
$\dot{q}$	=	Heat-flux
Re	=	Reynolds number/stress
s	=	Natural wall coordinate
T	=	Temperature
u, v, w	=	Velocity vector comp.
δ	=	Boundary-layer thickness
Δ_o	=	DES grid-filter
$\Delta(x, y, z)^+$	=	Non-dimensional coordinates
θ	=	Momentum thickness
$\tilde{\nu}$	=	S-A turbulence variable
ρ	=	Density
ω	=	Vorticity
$<>$	=	Root-mean-square
$'$	=	Instantaneous fluctuation (superscript)
$_\infty$	=	Freestream (subscript)
$_o$	=	Initial (subscript)
$_{w,n}$	=	Wall/normal (subscript)
$_{ref}$	=	Reference (subscript)

*Graduate Student, School of Aeronautics and Astronautics, Student Member AIAA
†Associate Professor, School of Aeronautics and Astronautics, AIAA Associate Fellow
‡Professor, School of Aeronautics and Astronautics, AIAA Associate Fellow

I. Introduction

The 1978 experimental study conducted by Deveikis and Bartlett [1] on supersonic wing-elevon cove boundary-layer ingestion highlighted characteristics of a practically interesting flow. The particular region of interest corresponds to the cove area between the wing and elevon, which is needed in order to allow for elevon deflection. The experimental study simulated flow over a full-scale model wing-elevon cove on the windward surface of the space shuttle orbiter. Supersonic flow was achieved with NASA Langley's 8-foot high-temperature structures blowdown wind-tunnel. The purpose of this experiment was to determine effects of hot boundary-layer ingestion during reentry, as a function of the cove exit-to-inlet area ratio. A total of 41 tests were done, varying cove exit-to-inlet area from 0 (sealed) to 1 (full leakage). Pressure and heat transfer data was obtained on both the cove and elevon surfaces using pressure orifices and thermocouples. For the majority of tests, the model was set to an angle of attack of 12°, with an elevon deflection of 15°. The freestream Mach number for all tests was 6.9, with a corresponding total temperature of 1888 K. The average primary freestream Reynolds number was 4.4e6 m^{-1}, although several tests were done with a lower average value of 1.3e6 m^{-1}. A small portion of tests also introduced a flow separator at the wing-elevon cove juncture, to study effects of full flow separation. Experimental results for the high Reynolds number attached-flow tests show that cove surface pressures were uniform, decreasing with area ratio, whereas cove surface heat-flux varied with distance into the cove, increasing with area ratio. For maximum area ratio, surface heat-flux inside of the cove ranged from 23% to 6% of the upstream wing surface heat-flux; accompanying surface pressure inside of the cove reached, at most, 20% of upstream wing surface pressure. Two important observations were made in the experimental study. The first is that the conditions in the cove environment are too severe for unprotected interior control surfaces. The second is that there are clear indications that convective heating in the cove is time-dependent, leading to significant additional aerothermal loading.

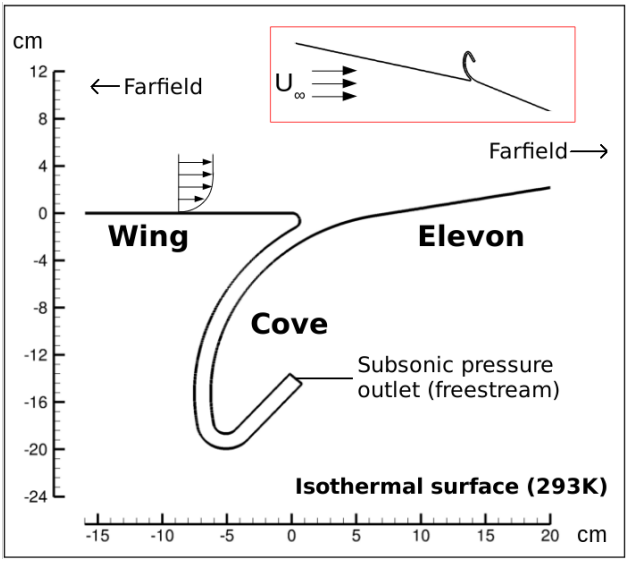

Fig. 1 Wing-elevon cove schematic.

An overview schematic of the experimental wing-elevon cove geometry is provided in Fig. 1, where the simulated flight reference frame of the experiment is displayed in the highlighted red box. The chord lengths of the wing and elevon were 124 cm and 69 cm, respectively, with a total span length of 105 cm. Aerodynamic fences on the sidewalls of the model were used to channel upstream surface flow across the cove entrance. The wing and elevon surfaces were covered with 1.27 cm thick Glasrock tiles for thermal protection, and data acquisition devices for surface pressure and heat transfer were embedded in the Glasrock surfaces. The diameter and area of the cove was 1.27 cm and 133.35 cm^2, respectively. The cove extended about 20 cm inside of the wing-elevon surfaces, before deflecting up. The end of the cove was either sealed, partially sealed, or fully open to permit/hinder flow exiting the cove to an outside cavity, near freestream pressure; this method was based on an early shuttle orbiter design for cove sealing. The geometry of the cove region is created about an axis of rotation, providing smooth control surface movement into and out of the cove. A more detailed diagram of the cove geometry can be found in the published experimental study [1]. To create fully turbulent flow at the cove entrance, the boundary-layer was tripped near the leading-edge with 0.24 cm diameter spheres. The average boundary-layer thickness for high Reynolds number tests was of the order of the cove diameter, δ_o = 2.16 cm.

This paper presents a computational investigation of supersonic wing-elevon cove boundary-layer ingestion, focusing on the time-dependent nature of the juncture and cove flow. Simulation of the Deveikis and Bartlett experimental study was done employing computational fluid dynamics (CFD). Specifically, wing-elevon cove flow was numerically computed with improved delayed detached eddy simulation (IDDES). The entire streamwise geometry of the experimental wing-elevon cove, and a portion of the span, is identically modeled; however, the cove exit is simplified slightly due to complexities produced by the experiment when achieving full cove area leakage. One particular test was simulated, corresponding to high Reynolds number attached-flow with maximum exit-to-inlet cove area ratio. The exit-to-inlet cove area ratio was chosen to represent full cove exit flow, for direct application to reusable supersonic vehicles.

This section provided the introduction and layout of the experimental study for the research presented in this paper. The methodology of the computational investigation is provided in Sec. II, which elaborates on the numerical methods and computational mesh employed. The results of the IDDES computations are presented in Sec. III. Time-averaged mean surface data are compared to published experimental results in Sec. IIIA, with comments on the numerical discrepancies. The flow structure is visualized through mean temperature and velocity contours in Sec. IIIB. Advection of turbulent momentum is displayed with planar Reynolds stresses in Sec. IIIC. Unsteadiness of the flow is visualized with instantaneous density gradient contours in Sec. IIID, where the low-frequency unsteady motions of the reattaching shear-layer and shock-foot oscillation are analyzed. Large coherent turbulent structures observed in the spanwise plane are presented and discussed in Sec. IIIE. Conclusions of the research done for this paper and intended future investigations are outlined in Sec. IV.

II. Methodology

The particular test that was simulated corresponds to fully turbulent, supersonic, high Reynolds number flow. The freestream conditions and boundary-layer properties for this test are provided in Table 1. Computational data were acquired with the CFD software CREATE-AV Kestrel. The mesh was produced with the grid creation software Pointwise. Post-processing of data, i.e. time-averaging, Reynolds stress calculations, and plotting, was done using the CFD visualization software Tecplot. Preliminary 2-D unsteady Reynolds-averaged Navier-Stokes (URANS) computations were done in order to obtain an understanding of the primary flow features, e.g. reattachment location, bow-shock angle, and unsteadiness, as well as to ascertain resolution requirements, such as Δy_w^+. Computational resources were provided by the U.S. Army Research Laboratory (ARL) high-performance computing cluster Excalibur. Excalibur uses Intel Haswell E5-2698 64-bit processors, which are clocked at 2.3 GHz and have 16 cores per CPU, with 2 CPUs per node. Preliminary URANS computations used a single node, with 32 cores. The IDDES computation used 200 nodes, with 16 ranks and 2 threads per node, for a total of 3400 cores.

M_∞	6.86
T_∞ (K)	221
P_∞ (Pa)	1930
Re_∞ (m^{-1})	4.29e6
q_∞ (Pa)	63577
δ_o (cm)	2.16
θ_o (cm)	0.20
Re_θ	8500

Table 1 Freestream and boundary-layer properties.

Turbulence was modeled with IDDES, which is an improvement of delayed detached eddy simulation (DDES). DDES switches between large eddy simulation (LES) in "focus" regions, and RANS otherwise. The RANS regions were modeled with the Spalart-Allmaras (S-A) turbulence model. Spatial and temporal accuracy is second-order, computed with the HLLE++ inviscid flux scheme, LDD+ viscous flux scheme, and Euler implicit time integration. Weighted least-squares cell-average gradient construction methods were used. Boundary conditions of control surfaces were modeled as cold (293.15 K) isothermal no-slip walls, per the experimental study. Boundary conditions in the spanwise direction are periodic and all other surfaces are farfield. The time-step was set to 1e-7 s, which corresponds to a non-dimensional time-step $u_\infty \Delta t/\delta_o$ = 9.3e-3. Surface data were sampled at every time step, f_s = 10 MHz. The computational domain was sliced normal to the streamwise plane, and -15° from the spanwise surface-normal plane,

for planar data extraction. These slices were sampled at f_s = 100 kHz and were used for mean and unsteady flow analysis. The total number of iterations was 100,000, with 3 sub-iterations, corresponding to 10 ms of physical time, 10 flow-through times, and a non-dimensional time of $u_\infty t/\delta_o = 926$. Time-averaging was done after 3 flow-through times, in order to avoid including transient phenomena in the data collection. The gas species used was air, and assumed to be thermally ($p = \rho RT$) and calorically ($e = C_v T$) perfect.

A. Computational Mesh

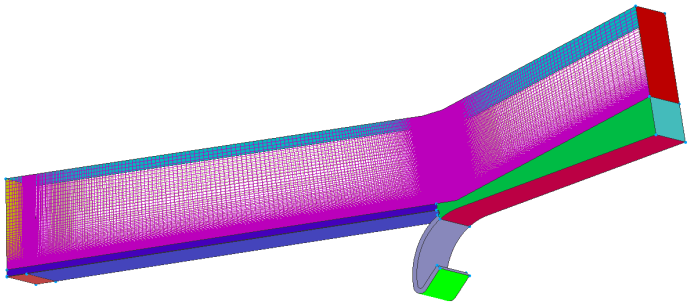

Fig. 2 Isometric view of the computational mesh.

Due to the complexity of the geometry, the mesh is constructed by a combination of several structured block-domains stitched together. Mesh development incorporated multiple progressions of the grid in order to determine optimal resolution and grid independence. The blocks are created with Spalart's recommendation for DES computations [2], and validated for LES computations [3]. Three distinct regions are outlined by Spalart for DES: the Euler region (ER), viscous region (VR), and focus region (FR). RANS is employed in the ER and VR blocks, whereas LES is employed in the FR blocks. Therefore, each block is created with careful consideration of the flow in that region. The ER blocks are far from the surface and the least-resolved. The VR blocks are resolved enough for near-wall RANS computations, with $\Delta y_w^+ \leq 1$. The exterior and interior (cove) FR blocks are highly-resolved for LES computations, with a constant DES grid-filter Δ_o = 5e-4 m, set by the spanwise grid spacing; in these blocks, $\Delta z^+ \approx 75$, $\Delta x^+ \approx 60$, and $\Delta y_w^+ \leq 1$. The ER block consists of 51x1001x301 points, the incoming flat-plate VR block consists of 401x201x301 points, the exterior FR block consists of 801x801x301 points, and the interior FR block consists of 401x901x301 points. Furthermore, the complete computational mesh is comprised of 3.4e8 cell-volumes. The spanwise length of the computational mesh is 15.12 cm, 14% of the experimental modal, and is centered at z = 0 cm. This length is approximately equal to $7\delta_o$, and is large enough to not cause issues for compressible turbulent boundary-layer simulations, per the high-fidelity computations of Poggie et al. [4].

B. Numerical Turbulence Formulations

Hybrid RANS/LES methods, such as DES, are favorable in that the computational cost for complex simulations is largely reduced. For near-wall and freestream calculations, the RANS equations are solved with the S-A turbulence model. The S-A turbulence model solves a one-equation transport equation for the S-A variable, $\tilde{\nu}$, which is used to find turbulent eddy viscosity, $\tilde{\nu}_t$ [5]. The transport of the S-A variable is modeled as follows*

$$\frac{\partial \tilde{\nu}}{\partial t} + u_j \frac{\partial \tilde{\nu}}{\partial x_j} = C_{b1}[1 - f_{t2}]\tilde{S}\tilde{\nu} + \frac{1}{\sigma}\{\nabla \cdot [(\nu + \tilde{\nu})\nabla\tilde{\nu}] + C_{b2}|\nabla\tilde{\nu}|^2\} - [C_{w1} f_w - \frac{C_{b1}}{\kappa^2} f_{t2}]\left(\frac{\tilde{\nu}}{d}\right)^2 + f_{t1}\Delta U^2. \quad (1)$$

The turbulent eddy viscosity is then obtained as a function of the S-A variable,

$$\nu_t = \tilde{\nu} f_{v1}. \quad (2)$$

*Elaboration on the various constants/functions that appear in Eq. (1) are left out for brevity, but are provided by Spalart and Allmaras [5].

DES switches between RANS computations of the transport equation and LES subgrid-scale formations by replacing the distance function, d, in Eq. (1) by a modified length-scale [6],

$$\tilde{d} = \min[d, C_{DES}\Delta_o]. \tag{3}$$

C_{DES} is a constant, commonly set to 0.65, and the grid-filter,

$$\Delta_o = \max[\Delta x, \Delta y, \Delta z], \tag{4}$$

is a function of the largest directional cell-size. The drawback to the original DES formation is that areas between RANS and LES regions, labeled "gray areas", produce numerical issues and grid-density dependence. In attached boundary-layers, as grid spacing is reduced to activate LES, the resolution is not sufficient to resolve internal velocity fluctuations, referred to as modeled-stress depletion [7]. This issue is corrected in the DDES formation [8], which uses a function f_d to detect attached boundary-layers, varying from 0 to 1. The length-scale is altered to

$$\tilde{d} = d - f_d \max(0, d - C_{DES}\Delta_o). \tag{5}$$

Further issues were found in the DDES formation by Travin et al. [9], where non-physical reductions in skin friction were observed in DDES computations of channel flow with highly-resolved grids. To solve this, IDDES was developed as a combination of DDES and wall-modeled LES [10]. The formation changes the evaluation of Δ_o, as well as the blending of the gray areas. The new grid-filter,

$$\Delta_{filter} = \min(\max[C_w d_w, C_w h_{max}, h_{wn}], \Delta_o), \tag{6}$$

is a modified largest directional cell-size function, which incorporates the wall-normal distance d_w and height of the cell in wall normal-direction h_{wn}. Furthermore, the IDDES length-scale is defined as

$$\tilde{d} = f_{hyb}(1 + f_{restore})d + (1 - f_{hyb})d_{LES}. \tag{7}$$

The function f_{hyb} acts in a similar manner to the DDES f_d. The additional LES length-scale in Eq. (7) is defined as

$$d_{LES} = C_{DES}\Psi\Delta_{filter}, \tag{8}$$

where the functions Ψ and $f_{restore}$ are defined by local boundary-layer flow parameters. Further elaboration on the IDDES formation can be obtained from Shun et al. [10].

III. IDDES Results

Research in separated flows has shown universal three-dimensionality and unsteadiness [11], with a large range of spectral content. The length scales associated with turbulence and unsteadiness lead to difficulties in computations of complex flows, with little research done on low-frequency shock movement [12]. Therefore, the primary focus of data analysis for this paper is on the low-frequency unsteady motions of the reattaching shear-layer and shock-foot oscillation. The results of the IDDES computation of the wing-elevon cove are presented to display both the generic flow structure and unsteadiness in the region. To compare results with experimental data, time-averaged mean surface pressure and heat-flux data are normalized and plotted with experimental data. The generic flow structure is provided with time-averaged flow parameter contours, displaying mean flow characteristics at the wing-elevon cove juncture and inside of the cove region. Reynolds stresses were calculated in order to display advection of turbulent momentum at wing-elevon cove juncture. Analysis and discussion of the low-frequency unsteadiness is provided with instantaneous density gradient contours in the same region. In addition to generic flow structure visualization and turbulent/unsteady analysis, observed large coherent turbulent structures in the spanwise surface-normal plane are subsequently presented. Preliminary URANS computations are mentioned throughout this section, to comment on the differences between IDDES results and lower-fidelity computations.

A. Surface Variable Comparison

Published experimental data include pressure and heat transfer data on the interior wing-elevon cove surfaces and the exterior elevon surface. Experimental uncertainty for the facility's thermocouple temperature readings are listed to be up to ± 9% [13]. No information is available for surface pressure uncertainty, and therefore is estimated to be ± 5% (95% confidence). Computational surface data were taken and averaged over time for comparison, with a sampling frequency of 10 MHz. To match published experimental data, surface pressure and heat-flux results were normalized by reference values obtained 2.54 cm upstream of the cove juncture. Reference surface pressure on the upstream wing is 10.16 kPa, and reference surface heat-flux is 205 kW/m^2. Tabulated data are provided with a distance variable, s, which represents a natural coordinate parallel to the interior cove wall and interior/exterior elevon wall. The interior cove surface pressure and heat-flux values are compared in Fig. 3a, where distance is measured into the cove region. The trends for computational surface pressure and heat transfer results follow those of experimental data, in that pressure is relatively constant and heat-flux decreases into the cove. Surface pressure inside of the cove was computed within 5-10% of experimental data, and surface heat-flux was computed within 5-30% of experimental data. The discrepancies between experimental and computational results for surface pressure and heat-flux are within normal expected computational uncertainties for complex flows [14, 15].

Surface pressure and heat-flux on the elevon interior/exterior surface are compared in Fig. 3b, focusing on the exterior surface data. For the elevon surface, the natural coordinate is measured starting inside of the cove moving outward. The exponential rise in surface variable data is attributed to the reattachment location at the wing-elevon juncture, located just outside of the cove environment. The time-averaged peak heat-flux magnitude and location were accurately obtained; the location was overpredicted by only 0.4 cm, and the magnitude was within 5% of experimental data. Surface pressure was accurately predicted in reattachment as well. The average peak heat-flux, occurring at reattachment, is located at s = 14.5 cm, with a magnitude 2.3 larger than the reference. It is important to note that the location and magnitude of peak heat-flux vigorously fluctuates, due to the unsteadiness of reattachment. Downstream of reattachment, surface pressure and heat-flux were overpredicted, with similar discrepancies to those displayed inside of the cove. At s = 32 cm, surface pressure matches experimental data perfectly, indicative of flow parameters approaching theoretical inviscid approximations. Heat-flux further downstream was expectedly overpredicted by about 15-20%.

The surface data displayed in Fig. 3 have been compared to preliminary time-averaged URANS computations (not shown here). Average differences in surface pressure between time-averaged URANS computations and IDDES results did not exceed 5% on the interior and exterior surfaces. Surface heat-flux displayed 10% average difference inside of the cove environment, and at most 20% difference on the elevon surface (in reattachment). These differences are within the same range of the discrepancies between IDDES and experimental results.

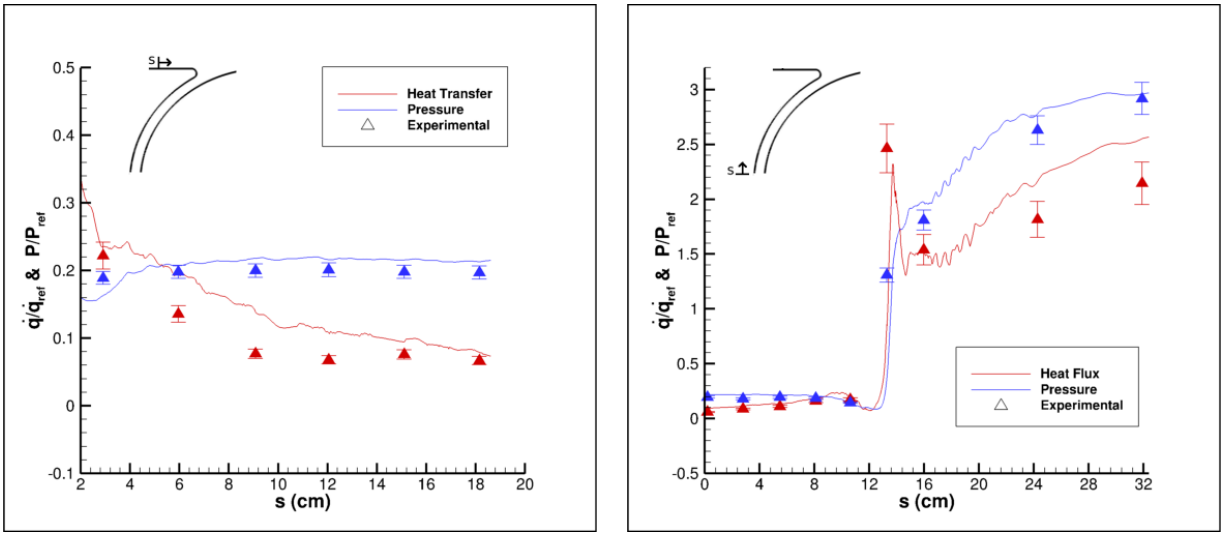

(a) Interior cove surface **(b) Interior/exterior elevon surface**

Fig. 3 Mean surface pressure and heat-flux comparison with experiment.

B. Mean Flow Visualization

The time-averaged mean flow structure at the wing-elevon juncture and cove environment is displayed in Fig. 4. Computational data were obtained with a normal-plane slice at the centerline of the domain, $z = 0$ cm. Time-accurate data were sampled with at a frequency of 100 kHz, and averaged after 3 flow-through times. Visualization of the entire cove environment is shown in Fig.4a. The temperature contour of the cove environment displays the hot boundary-layer ingestion into the cove. The localized packet of low-temperature inside the cove environment is attributed to a small separation vortex. Temperatures inside of the cove reach a near-constant equilibrium value of 900 K, which corresponds to approximately 39% of the total temperature. Experimental cove temperatures reached 37% of the total temperature. The reattaching bow-shock creates exceedingly high temperatures of 1400 K, which is approximately 60% of the total temperature. Reported experimental cove temperatures reached 50% of the total temperature near the cove entrance. It is noted in the experimental study that equilibrium was not achieved at the end of the test run, and temperatures should be considered minimum possible values.

The local wing-cove juncture flow structure is displayed in Fig. 4b. The flow in this region is similar to that of a backwards-facing step (BFS), where the boundary-layer separates and creates a free-shear layer which expands and reattaches at the downstream surface. The inclusion of the cove environment complicates the flow structures, allowing reverse flow in separation to continue into the cove, rather than to recirculate in the primary separation vortex. This behavior creates flow divergence at reattachment, which produces an elevated separation vortex attached to the wing-cove surface. As the flow turns around this vortex, it accelerates into the cove, and creates a secondary vortex inside of the cove. These vortices, however, are highly time-dependent and unsteady. The mean reattachment location is located 2.95 cm downstream of the wing-cove surface, which corresponds to the flow divergence location; this location overpredicts the experimental reattachment location by 0.4 cm. The reattachment location oscillates back and forth on the elevon surface as a result of the flapping shear-layer motion. This unsteady motion is coupled with breathing of the primary separation vortex attached to the wing-cove surface. The mean separation vortex engulfs the majority of the cove entrance, allowing a portion of the detached boundary-layer into the cove near the elevon surface. The velocities inside of the cove reach a maximum of nearly half of the freestream velocity, directly after turning at reattachment; however, as a result of the high temperatures inside of the cove, the mean flow is primarily subsonic.

The mean flow structure displayed in Fig. 4 was compared to preliminary time-averaged URANS computations. This was done throughout the IDDES computational run, for determination of achieved statistically significant, “steady-state”, flow. Comparison between final IDDES results and URANS computations displayed nearly identical mean flow structures; however, URANS computations predicted the reattachment location to be 0.5 cm farther downstream. In addition, the separation vortex attached to the wing-elevon surface was larger in size for URANS computations, and the interior cove vortex formed was shifted upstream from IDDES results.

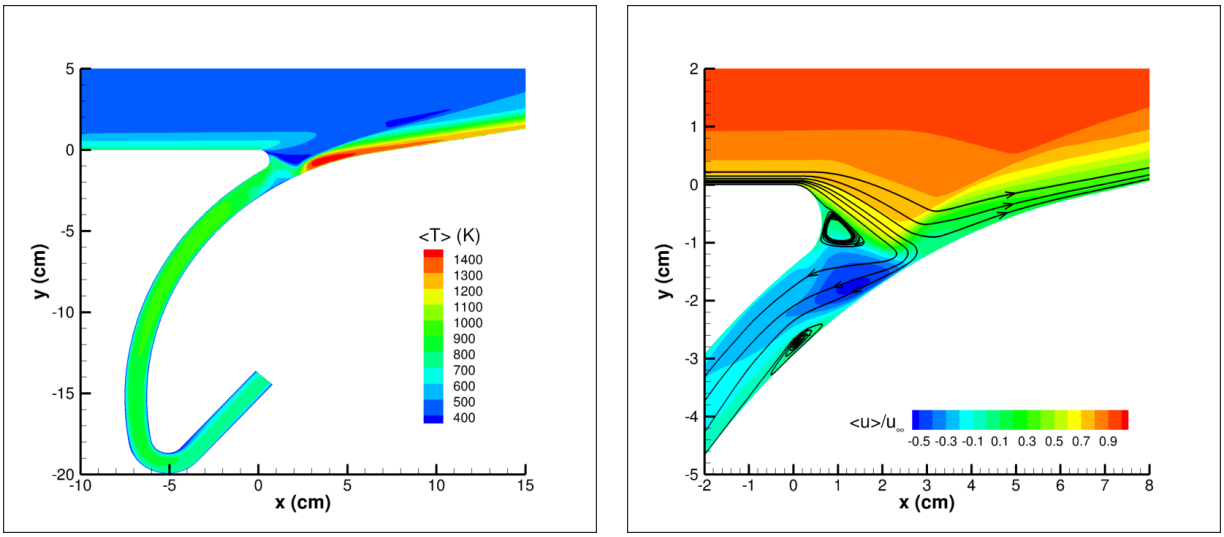

(a) Mean temperature **(b) Mean streamwise velocity**

Fig. 4 Mean cove environment and wing-elevon juncture flow structure contours.

C. Reynolds Stresses

The mechanism in which unsteady motion affects the mean-flow can be characterized by the root-mean-square (RMS) velocity fluctuations [16], or mean Reynolds stresses. Therefore, to analyze the advection of turbulent momentum, Reynolds stresses were calculated with the streamwise, wall-normal, and spanwise RMS velocity fluctuations. The normal turbulent stresses are displayed in Figs. 5a-5c, and the turbulent shear stress is displayed in Fig. 5d. The maximum RMS velocity fluctuations in the x-y plane clearly indicate the location the reattachment bow-shock, which is distinctly above the elevon surface. The development of the reattaching shear-layer is shown with lower RMS magnitude, which is on par with previous research on reattaching shear-layer unsteadiness in BFS flows [17]. In contrast to research on reattaching shear layers [18], the spanwise RMS velocity fluctuations display a distinctly different structure than those in the x-y plane. Interestingly, maximum spanwise RMS velocity fluctuations grip the surface of the wing-cove wall. The Reynolds shear stress in the x-y plane expectantly show negative correlation in RMS velocity fluctuations, characteristic of the turbulent transport of eddies. Inside of the cove region, however, a localized packet of velocity fluctuations are shown to be positively correlated. All Reynolds stresses display non-zero values immediately inside of the cove, reaching zero values further into the cove. This behavior is similar to that of published research on turbulent channel flows by Scotti et al. [19], who suggest that the unsteady fluctuations caused by pressure gradients only penetrate a certain length of a channel. In addition, non-zero values are seen downstream of reattachment, which is similar to the behavior shown for supersonic BFS flow [17].

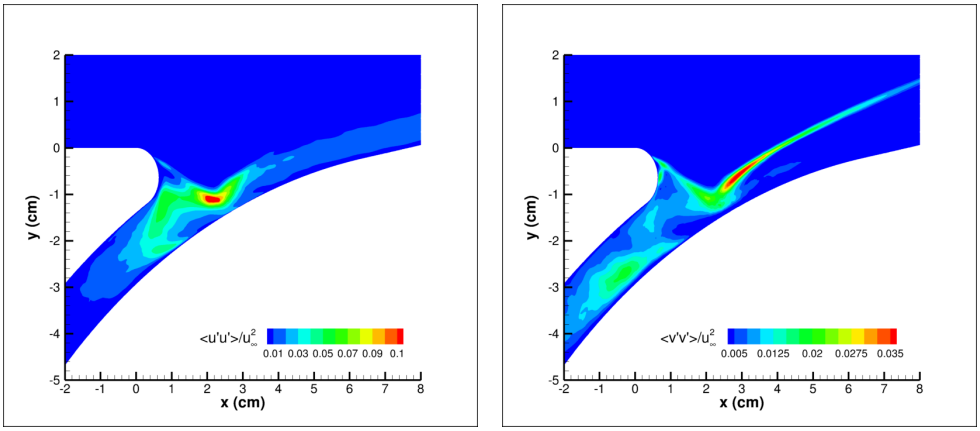

(a) Re_{11} **(b) Re_{22}**

(c) Re_{33} **(d) Re_{12}**

Fig. 5 Reynolds stress tensor contours.

D. Low-Frequency Unsteadiness

The unsteadiness of supersonic reattaching shear-layers has been previously researched [20]-[24], which attributes large-scale, low-frequency unsteadiness to large-scale turbulent structures in the separated shear-layer. The low-frequency unsteadiness produces a vertical flapping motion of the shear-layer, which induces an oscillatory motion of the reattaching shear-layer impingement point and shock-foot [12]. Furthermore, Eaton et al. [20] suggest that this low-frequency motion is caused by an instantaneous imbalance between the entrainment rate from recirculation and reinjection rate near reattachment. Additional attributions to the low-frequency motion include the bounded separation bubble breathing [20]. Unlike the research on reattaching shear-layers, the introduction of the cove region introduces a cavity region with an imposed subsonic boundary condition. Clemens [11] notes that this can cause flow unsteadiness to be coupled to fluctuations at the channel exit, which is applicable as the cove flow is, for the most-part, entirely subsonic.

To analyze the low-frequency unsteady motions, time-accurate density gradient contours were produced to mimic commonly produced Schlieren images. Analysis of the wing-elevon cove juncture flow-field, over the complete simulation time, was done with use of animated planar slices. Slices were sampled at a frequency of 100 kHz, over a total computational flow time of 10 ms, allowing the capture of low-frequency unsteady motions. In the LES region, the steady-state mean turbulent boundary-layer immediately breaks down into unsteady turbulent flow. The Kelvin-Helmholtz instability results in the formation of large vorticies in the detached shear-layer, which continuously propagate downstream. Various distinct unsteady flow features were observed, including the oscillatory behavior of the reattaching shear-layer impingement point and shock-foot. The time-scale of this behavior is on the order of half of a millisecond, corresponding to a Strouhal number, based on boundary-layer thickness, near 0.03, which is indicative of low-frequency shear-layer flapping and shock-foot oscillation [12]. In addition to the low-frequency movement of the shock-foot and shear-layer, disturbances in the reattachment bow-shock are observed. The disturbances display a section of the recirculation flow cutting-off from reattachment, via large turbulent structures in the shear-layer, propagating downstream. This behavior is characterized by McGuinness [25] as a "divorced eddy". Aside from the low-frequency unsteadiness in the wing-elevon cove juncture, the cove region itself exhibits high-frequency turbulent behavior. This behavior displays non-periodic motion, where numerous acoustic waves and reflecting expansion/compression waves are observed as flow travels through a large portion of the cove region. The high-frequency turbulent motions are produced by unsteady pressure gradients inside of the cove, as described by Scotti et al. [19], and is dually affected by the low-frequency motion at reattachment. This section's focus, however, is on the low-frequency unsteadiness of the wing-elevon cove juncture, and leaves the high-frequency turbulence in the cove environment for future investigation.

The periodic low-frequency unsteadiness of the reattaching shear-layer and shock-foot oscillation are displayed in Fig. 6. Instantaneous density gradient contours, in grayscale to mimic Schlieren photography, are provided over a time-span of 0.3 ms. Starting at $t = 6.525$ ms, Fig. 6a shows shear-layer impingement, denoted i', far above the downstream elevon surface. The distortion of the reattaching bow-shock, denoted i'', begins at this time. As a result, an increase of mass flux is induced into the cove. Elevon surface heating reaches minimal values, with no clear indication of peak surface heat-flux. After 0.025 ms, Fig. 6b, shear-layer impingement is forced downward to the elevon surface, clearly displacing the shock-foot, further distorting the reattachment bow-shock. Large turbulent structures are observed post-reattachment between the reattachment bow-shock and elevon surface. At this time, maximum peak surface heating, 1.4 times the mean value, is observed on the elevon surface at the shock-foot location. Inside of the cove region, this motion produces instantaneous reflection shocks downstream of the cove entrance. Another 0.025 ms later, Fig. 6c, the shock-foot shifts upstream, which also shifts the location of peak surface heating, with a decreased magnitude of 1.1 times the mean value. The divorcing eddy is now seen as the distortion in the bow-shock moves further downstream, displayed in the region between i'' and i'''. The turbulent structures seen at the previous time are also shown to be propagating downstream with this distortion. This distortion continues to propagate downstream, and higher-frequency unsteady motions at the wing-elevon cove juncture are observed. The last frame, Fig. 6d, displays the flow returning to a more steady formation, which lasts roughly 0.1 to 0.2 ms, before the oscillatory low-frequency unsteadiness begins again. At this location, the shock-impingement is also above the surface wall, and peak surface heat-flux location and magnitude are near mean values.

As speculated by the experimental study [1], the time-dependent nature of wing-elevon cove juncture flow produces large fluctuations in surface pressure and heat-flux, visualized with the vertical motion of the shear-layer impingement and shock-foot oscillation. This low-frequency unsteadiness is extremely important to characterize, as intense fluctuations caused by shock oscillation lead to aircraft fatigue and aerothermal loading [21]. The hostility of the cove environment is visualized with the chaotic high-frequency turbulence displayed in the cove region. Furthermore, the flow behavior in this region definitively would be too severe for unprotected interior surfaces.

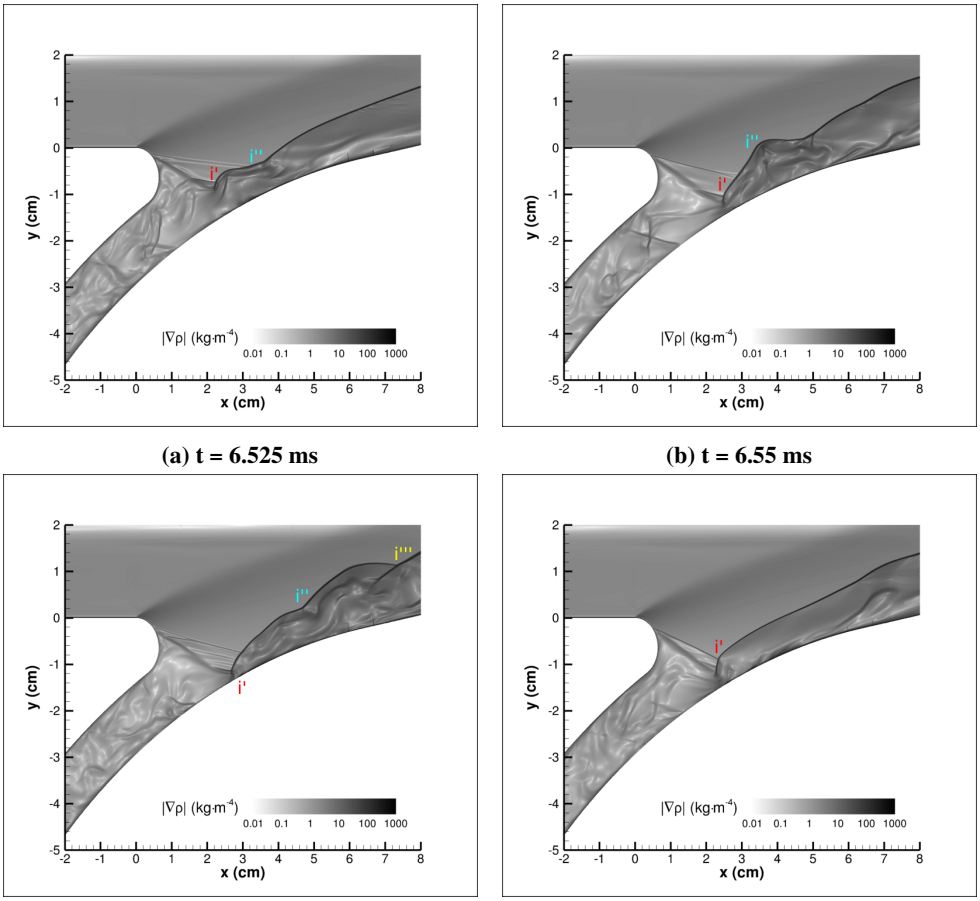

(a) t = 6.525 ms **(b) t = 6.55 ms**

(c) t = 6.575 ms **(d) t = 6.85 ms**

Fig. 6 Instantaneous density gradient contours.

E. Coherent Vortical Structures

Coherent vortical structures in turbulent flows can form due to fixed flow instabilities, such as the Kelvin-Helmholtz instability in reattaching shear-layer flows [26]. Immediately downstream of reattachment, coherent vortical structures were observed in the spanwise surface-normal plane. These structures appear to consist of counter-rotating Görtler-type vortices. Görtler-type structures are comprised of periodic counter-rotating vorticies, formed from centrifugal instabilities, which have been observed in hypersonic compression-ramp flows [27]. These structures are known to originate in the shear-layer, as a result of the streamline curvature [28]. The appearance of these structures displays the three-dimensionality of the flow downstream of reattachment. To visualize the vortical structures in the spanwise direction, planar slices were taken in the z-y plane, at -15° from the spanwise surface-normal plane. These slices were sampled at the same frequency as the streamwise normal slices, 100 kHz. Fig. 7 displays an instantaneous vorticity magnitude contour in this plane. The surface-normal distance, y_n, and spanwise distance, z, are normalized by the boundary-layer thickness at the reference location. This normalization is done to correspond with LES spatial resolution requirements [4]. The dividing region between the high and low vorticity represents the local boundary-layer thickness. The regions of maximum vorticity show the formation of the counter-rotating vorticies, which are enhanced in Fig. 7. These structures exhibit unsteadiness in the size and the amount of structures present at any given time. During the distortion of the reattachment bow-shock, the local boundary-layer thickness varies, and as a result, some of these structures grow larger than what is displayed. In general, these structures were observed to be approximately steady throughout the duration of computational time. It is noted that the experimental study did not mention the existence of such structures. Navarro-Martinez et al. [27] have shown that exceedingly high surface heating can be attributed to Görtler-type structures, which is corroborated by Cao et al. [28] Therefore, to further characterize this flow, the Görtler-type structures that appear are considered highly-important for future investigation.

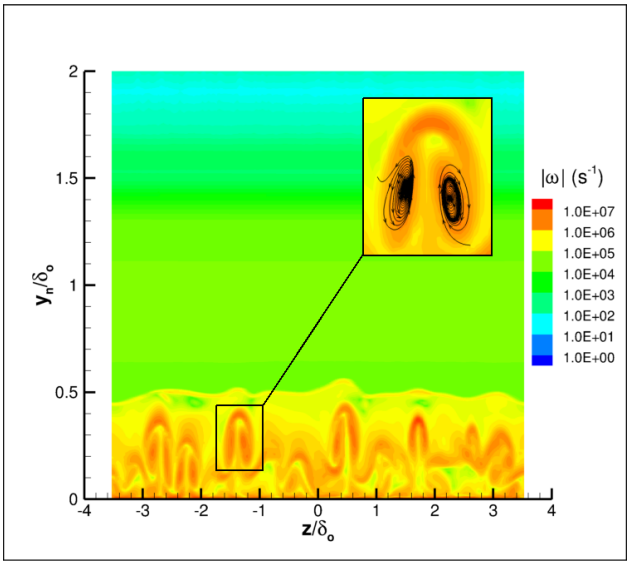

Fig. 7 Instantaneous streamwise vorticity contour; Görtler-type vortices.

IV. Concluding Remarks

Results from the IDDES computation of the wing-elevon juncture and cove environment provide useful insight for supersonic flow in this region. Computed surface data were compared to experimental results, showing reasonably good agreement. Mean flow results were provided to visualize the hot boundary-layer ingestion and flow structure at the wing-elevon juncture. Reynolds stresses at the wing-elevon juncture provide visualization of the turbulent momentum flux, corresponding to the reattaching shear-layer and reattachment bow-shock. The unsteadiness of the wing-elevon juncture was visualized with instantaneous density gradient contours. Lastly, large coherent vortical structures downstream of reattachment were shown to consist of Görtler-type vortices. The Deveikis and Bartlett experimental study observed that flow through the cove produces a hostile environment, and that convective heating was time-dependent. Both observations are replicated in the IDDES results, and further expanded upon. The cove environment exhibits chaotic high-frequency turbulence, with high levels of convective heating. The time-dependent nature of the flow was displayed with low-frequency unsteadiness of the shear-layer impingement and shock-foot oscillation. This unsteadiness produces large fluctuations in surface variables, which can lead to surface fatigue and intense aerothermal loading [21].

This paper serves as a visualization of the turbulent flow structure and unsteadiness of the wing-elevon juncture and cove environment. As a continuation of the research presented in this paper, intensive analysis of the unsteadiness in this region will be performed on the IDDES results. First, spectral analysis of the surface heat-flux and pressure on the interior cove and exterior elevon surfaces will be done. A large focus of this analysis will be on the reattachment region. Power spectral density (PSD) calculations will allow for more detailed evaluation of the frequencies involved in this flow. Furthermore, the low-frequency motions of the shear-layer impingement and shock-foot oscillation will be investigated in more depth. The high-frequency turbulence inside of the cove environment will be also be a large portion of unsteady data analysis. Three-dimensional turbulence of the flow in the wing-elevon juncture and cove environment will be analyzed with use of constant Q-Criterion iso-surfaces, providing more comprehensive instantaneous flow visualization. In addition, the coherent Görtler-type vortical structures will be analyzed further, such as with use of two-point correlations. These structures were not previously researched by the experimental study, and thus are considered to be highly-important and will be a major focus of future investigation.

Acknowledgments

The present work was supported by AFRL under the “Reusable Hypersonic Vehicle Structures” project, Contract FA8650-18-c-2253. Computational resources were provided by the AFRL DSRC and by Information Technology at Purdue, West Lafayette, Indiana. Cleared for public release on April 27, 2020 under case number 88ABW-2020-1538.

References

[1] Deveikis, W. D., and Bartlett, W., "Pressure and Heat-Transfer Distributions in a Simulated Wing-Elevon Cove With Variable Leakage at a Free-Stream Mach Number of 6.9," Technical Report NASA TM-74095, Nasa Langley, 1978.

[2] Spalart, P., "Young-Persons Guide to Detached-Eddy Simulation Grids," NASA CR-2001-211032.

[3] Georgiadis, N., Rizzetta, D., and Fureby, C., "Large-Eddy Simulation: Current Capabilities, Recommended Practices, and Future Research," *AIAA*, Vol. 48, No. 8, 2010, pp. 1772–1784. doi:10.2514/1.J050232.

[4] Poggie, J., Bisek, N., and Gosse, R., "Resolution Effects in Compressible, Turbulent Boundary Layer Simulations," *Computers and Fluids*, Vol. 120, 2015, pp. 57–69.

[5] Spalart, P., and Allmaras, S., "A One-Equation Turbulence Model for Aerodynamic Flows," *AIAA*, Vol. 439, 1992. doi: 10.2514/6.1992-439.

[6] Spalart, P., Jou, W., Stretlets, M., and Allmaras, S., "Comments on the Feasibility of LES for Wings and on the Hybrid RANS/LES Approach," *AFOSR International Conference on DNS/LES*, 1997.

[7] Spalart, P., "Detached-Eddy Simulation," *Annual Review of Fluid Mechanics*, Vol. 41, 2009, pp. 181–202.

[8] Spalart, P., Deck, S., and Shur, M., "A New Version of Detached-Eddy Simulation, Resistant to Ambiguous Grid Densities," *Theoretical Computational Fluid Dynamics*, Vol. 20, 2006, pp. 181–195.

[9] Travin, A., Shur, M., and Strelets, M., "Improvement of Delayed Detached Eddy Simulation for LES with Wall Modeling," *European Conference on Computational Fluid Dynamics*, 2006.

[10] Shur, M., Spalart, P., Strelets, M., and Travin, A., "A Hyrbrod RANS-LES Approach with Delayed-DES and Wall-Modeled LES Capabilities," *International Journal of Heat and Fluid Flow*, Vol. 29, 2008, pp. 1638–1649.

[11] Clemens, N., and Narayanaswamy, V., "Low-Frequency Unsteadiness of Shock Wave/Turbulent Boundary Layer Interactions," *Annual Review of Fluid Mechanics*, Vol. 46, No. 1, 2014, pp. 469–492.

[12] Leger, T., Bisek, N., and Poggie, J., "Detached-Eddy Simulation of a Supersonic Reattaching Shear Layer," *AIAA*, Vol. 55, No. 11, 2017, pp. 3722–3733. doi:10.2514/1.J056103.

[13] Johnson, C., and Taylor, A., "Heat-Transfer and Pressure Measurements on a Simulated Elevon Deflected 30° Near Flight Conditions at Mach 7," Technical Report NASA TM X-3563, Nasa Langley, 1977.

[14] Dolling, D., "Fifty Years of Shock-Wave/Boundary-Layer Interaction Research: What Next?" *AIAA Journal*, Vol. 39, 2001, pp. 1517–1531. doi:10.2514/2.1476.

[15] Bose, D., Brown, J., Gnoffo, P., Johnston, C., and Hollis, B., "Uncertainty Assessment of Hypersonic Aerothermodynamics Prediction Capability," *Journal of Spacecraft and Rockets*, Vol. 50, No. 1, 2013, pp. 12–25.

[16] Pope, S., *Turbulent Flows*, Cambridge University Press, Cambridge, United Kingdom, 2000.

[17] Logan, R., Ranjan, R., and Gaitonde, D., "Unsteadiness in a Supersonic Backward-Facing Step Flow," *AIAA Aviation Forum*, 2019. doi:10.2514/6.2019-3343.

[18] Deshpande, A., and Poggie, J., "Unsteadiness in a Compressible Reattaching Shear Layer," *AIAA SciTech Forum*, 2019. doi:110.2514/6.2019-1874.

[19] Scotti, A., and Piomelli, U., "Numerical Simulation of Pulsating Turbulent Channel Flow," *Physics of Fluids*, Vol. 13, No. 5, 2001, pp. 1367–1384. doi:10.1063/1.1359766.

[20] Eaton, J., and Johnston, J., "Low-Frequency Unsteadyness of a Reattaching Shear Layer," *Turbulent Shear Flows 3*, 1982, pp. 162–170.

[21] Poggie, J., and Smits, A., "Shock Unsteadiness in a Reattaching Shear Layer," *Journal of Fluid Mechanics*, Vol. 429, 2001, pp. 155–185. doi:10.1017/S002211200000269X.

[22] Driver, D., Seegmiller, H., and Marvin, J., "Time-Dependant Behavior of a Reattaching Shear Layer," *AIAA*, Vol. 25, No. 7, 1987, pp. 914–919. doi:10.2514/3.9722.

[23] Poggie, J., "Large-Scale Structures in Implicit Large-Eddy Simlation of Compressible Turbulent Flows," *AIAA*, 2014.

[24] C., H., Settles, G., Williams, D., and Bogdonoff, S., "A Reattaching Free Shear Layer in Compressible Turbulent Flow," *AIAA*, Vol. 20, No. 1, 1982, pp. 79–85. doi:10.2514/3.51049.

[25] McGuinness, M., "Flow with a Separation Bubble - Steady and Unsteady Aspects," Ph.D. thesis, Cambridge University, Cambridge, United Kingdom, 1978.

[26] Fiedler, H., "Coherent Structures in Turbulent Flows," *Progress in Aerospace Sciences*, Vol. 25, No. 3, 1988, pp. 231–269. doi:10.1016/0376-042188900012.

[27] Navarro-Martinez, S., and Tutty, O., "Numerical Simulation of Gortler Vortices in Hypersonic Compression Ramps," *Computers and Fluids*, Vol. 34, 2004, pp. 225–247.

[28] Cao, S., Klioutchnikov, I., and Oliver, H., "Gortler Vortices in Hypersonic Flow on Compression Ramps," *AIAA Journal*, Vol. 57, No. 9, 2019, pp. 3874–3884. doi:10.2514/1.J057975.